# Port Controlled Hamiltonian Modelling and IDA-PBC Control of Dual Active Bridge Converters for DC Microgrids

Sriram K. Gurumurthy, *Student Member, IEEE*, Marco Cupelli, *Senior Member, IEEE*, Siddharth K. Bhanderi, Antonello Monti, *Senior Member, IEEE*, Philipp Joebges, *Student Member, IEEE,* Zhiqing Yang, *Student Member, IEEE* and Rik W. De Doncker, *Fellow, IEEE*

***Abstract*— Power electronics based Medium-Voltage Direct Current (MVDC) Microgrids consist of several interconnected feedback-controlled switching converters. Such systems experience bus voltage stability challenges owing to the negative incremental resistance of Constant Power Loads (CPLs) and converter control loop interactions. To tackle the stability challenges, this paper presents the application of the Interconnection and Damping Assignment Passivity Based Control (IDA-PBC) approach to the Port-Controlled Hamiltonian (PCH) model of Dual Active Bridge (DAB) source-side converters in a MVDC Microgrid. For the DABs, a Fundamental Average Model (FAM) approach considering Phase Shift Modulation (PSM) is provided and used for deriving the corresponding IDA-PBC control law. We analyze the effectiveness of the controller on large signal scenarios considering disturbances such as load step up, and DAB disconnection. Hardware-in-the-Loop (HiL) experiments using Opal-RT and Labview FPGAs, as well as, low power prototype tests are carried out to demonstrate the validity and feasibility of the proposed approach.**

***Index Terms*— DC-DC power converters, power generation control, voltage control, stability, Nonlinear control systems, Microgrids**

## I. Introduction

DC power systems are considered to be solutions for scenarios that require high power conversion efficiency such as renewable power integration, industrial grids, marine power systems and Microgrids [1]-[4].

The use of the single-phase Dual Active Bridge (DAB) topology for MVDC Microgrids, referred to as DAB throughout the text, offers various advantages over non-isolated DC-DC converters such as galvanic isolation and soft switching [5]. Furthermore, the DAB offers high power density, bidirectional power flow capabilities and buck/boost operation [5].

The advantages of DC distribution for different applications have been provided in [1]-[4], and in particular, the benefits related to the DAB in MVDC grids [6] can be summarized as:

1) Enhanced efficiency, DAB power conversion stages reach an efficiency close to *99%*
2) Size, weight and cost reduction in distribution cables and magnetic components
3) Paralleling of power sources does not require time-critical phase matching

When analyzing a DC power electronic system from the DC bus, the load converters, often called Point of Load (POL) converters, operate under closed-loop output voltage control. Due to the tight regulation, the POLs behave as Constant Power Loads (CPLs) within their control-loop bandwidth [9]. These CPLs exhibit the negative incremental input resistance characteristics, which is the origin of the undesired destabilizing effects in the system [10], [25]. Conditions under which the instability takes place and methods for the stability analysis of DC power electronic systems have been reviewed and discussed in [26]. The stability problem can be explained in two ways. The first explanation considers the stability problem as a consequence of the previously described CPL behavior of the load converters. References [4]-[8], [28] provide possible control solutions to the CPL stability problem. The second explanation considers the instability as arising from adverse interactions of the different converters and their respective control loops [9], [26]. This instability can be handled, in the small signal sense, by impedance shaping [29].

The control of the DAB has received attention in several works, which have focused on linear control in [6], [11]-[14] and in [15] with a non-linear control law. To control a DAB based Microgrid, this paper focus on Passivity Based Control (PBC), which utilizes the structural properties of the physical systems to achieve a control law that is easy to implement [16], [17], [18]. PBC modifies the energy dissipation of the system through injection of virtual resistances, e.g. by Interconnection and Damping Assignment (IDA), which reduces the system oscillations and ensures the passivity of the closed loop system. An important characteristic of IDA-PBC

This work was supported in part by the BMBF (German Federal Ministry of Education and Research) under Grant 03EK3566B (DC-Direkt). (Corresponding author: Marco Cupelli)

The authors are with the Institute for Automation of Complex Power Systems, E.ON Energy Research Center, RWTH Aachen University, 52062 Aachen, Germany, and also with the Institute for Power Generation and Storage Systems, E.ON Energy Research Center, RWTH Aachen University, 52062 Aachen, Germany (e-mail: mcupelli@eonerc.rwth-aachen.de)

is that the passivity is preserved in arbitrary interconnections. That is, if a group of passive subsystems is interconnected through parallel or feedback, the resulting system is also stable and passive [19]. Thus, this passivity-by-design approach allows to configure the control for each subsystem individually; while guaranteeing large signal stability for the interconnected system. The IDA-PBC methodology found recently application on the stabilization of MVDC grids under the influence of CPLs for buck-boost [16], buck [17] and was applied for a solid-state transformer in [18]. A drawback of the existing results presented in [16], [17], [18] is that all of them require the knowledge of the power extracted by the CPL, which depending on the application case might be difficult to measure. A solution to this problem was presented by designing a load estimator and performing an adaptive control law based on the behavior of the buck-boost converter in [20]. The proposed approach requires only local current measurements for control synthesis.

Although the authors in [18] presented the first Port-Controlled Hamiltonian (PCH) model of the DAB, their approach is only valid for low power applications. They modeled the DAB as a sine wave inverter with unity modulation index and a boost rectifier (formed by the transformer leakage inductance and output H-bridge of the DAB) while operating under Sine Pulse-Width Modulation (SPWM). For high power applications, the Phase Shift Modulation (PSM) is used instead of the SPWM; the reason for this is that SPWM leads to higher switching losses since the carrier frequency is much higher than the fundamental frequency in the AC link of the DAB. Hence, a DAB modelling approach based on PSM is considered in this work; namely, the Fundamental Averaged Modelling (FAM) [5]. The FAM favors simplicity and is used to derive a compact IDA-PBC control law by means of the PCH framework.

The following contributions are presented in this paper:

1) Derivation of a non-linear IDA-PBC control law for the DAB under PSM operation with only local current measurements and without the knowledge of the load power,
2) Application of the IDA-PBC control law to address voltage regulation issues and guaranteeing large signal stability based on the passivity property,
3) Study the effectiveness of the FAM to represent the DAB behavior for IDA-PBC system level control design,
4) Feasibility proof of the proposed control approach, by carrying out Hardware-in-the-Loop (HiL) experiments using Opal-RT and Labview-FPGAs, as well as, low power prototype tests.

This paper is organized as follows: Section II introduces the PCH framework and the IDA-PBC design methodology applied to DC power electronic systems. Section III introduces the DAB PCH model, applies the IDA-PBC design on it and lays out the corresponding small signal analysis. Based on the small signal analysis practical bounds for the damping injection are defined. Section IV explains the circuit representation of the IDA-PBC method. The experimental HiL results of the proposed approach are presented in section V and low power prototype tests are presented in Section VI. In Section VII, a passivity analysis in the frequency domain and the Region of Attraction (ROA) for the proposed approach are presented.

## II. IDA-PBC Design

In this section, we briefly present the basics of the PCH modelling framework and its application to DC power electronics systems, which enables the derivation of the correspondent IDA-PBC control laws. Power converters transform the electric energy at their input port to deliver the energy required by the system connected at the output port. Therefore, the control goal can be seen as shaping the energy transferred between input and output ports, which is known as energy shaping control. The general form of a PCH model of a generic DC-DC converter is described by (1) and (2) [21]:

$$\frac{d\boldsymbol{X}}{dt} = \left(\boldsymbol{j}(\boldsymbol{X},\delta) - \boldsymbol{r}(\boldsymbol{X})\right)\frac{\partial H}{\partial \boldsymbol{X}} + \boldsymbol{g}(\boldsymbol{X},\delta)u \tag{1}$$

$$y = \boldsymbol{g}^{\boldsymbol{T}}(\boldsymbol{X},\delta)\frac{\partial H}{\partial \boldsymbol{X}}(\boldsymbol{X}) \tag{2}$$

$$x_1 = q_c = Cv\ ;\ x_2 = \phi_L = Li \tag{3}$$

The control input $\delta$ can represent the PWM duty ratio of generic DC-DC converter [21]; in the remainder of this paper $\delta$ represents the phase shift between the primary and secondary bridges for the DAB. Passive elements like inductances and capacitors can store energy in form of the magnetic flux and electrical charge, respectively. In equation (1), $\boldsymbol{X}$ is a column vector consisting of the *energy variables* that can be measured or observed. $\boldsymbol{H}$ is the *Hamiltonian of the system*, which is defined by each energy storage element in the system and therefore represents the total stored energy function. To be consistent with the PCH formulations in literature [21], we use the notation presented in (3). The *input vector* is represented by $(\boldsymbol{X}, \delta)$, which contains the external voltage and current sources. The port power variables are denoted by the input $u$ and output $y$. The energy storing passive elements form the overall PCH system by power preserving interconnections between them (i.e. by fulfillment of KVL and KCL). The interconnection structure between all storage elements is captured by the antisymmetric *interconnection matrix* $\boldsymbol{j}(\boldsymbol{X}) = -\boldsymbol{j}^{\boldsymbol{T}}(\boldsymbol{X})$. The resistive elements present in the system are represented by the so called positive definite *damping matrix* $\boldsymbol{r}(\boldsymbol{X}) = \boldsymbol{r}(\boldsymbol{X})^T > 0$, this would include also the CPLs, which can be represented as negative incremental resistances.

The goal of the IDA-PBC approach is to design a state-feedback control $\delta = \beta(\boldsymbol{X})$ such that the closed loop system dynamics can be represented in PCH form, as specified in (4), while stabilizing the system around a desired equilibrium $\boldsymbol{X}^*$. This goal is achieved by assigning a desired energy function $H_{\underline{\boldsymbol{d}}}$ of the closed loop system via the modification of the interconnection and damping matrices. The desired equilibrium $\boldsymbol{X}^*$ in a DC Microgrid, can be e.g. the reference value of the bus voltage.

$$\frac{d\boldsymbol{X}}{dt} = \left(\boldsymbol{j}_{\underline{d}}(\boldsymbol{X},\delta) - \boldsymbol{r}_{\underline{d}}(\boldsymbol{X})\right)\frac{\partial H_{\underline{d}}}{\partial \boldsymbol{X}} \tag{4}$$

The subscript $\underline{d}$ stands for the desired quantity, $\boldsymbol{j}_{\underline{d}}(\boldsymbol{X})$ is the desired antisymmetric interconnection matrix, while $\boldsymbol{r}_{\underline{d}}(\boldsymbol{X})$ is the desired positive semidefinite damping matrix. To be able to stabilize (1) on a desired equilibrium point $\boldsymbol{X}^*$, the desired energy function of the closed loop system $H_{\underline{d}}$ must have a strict local minimum at the desired equilibrium point [21]. The procedure described by the authors of [21], proved that for given $\boldsymbol{j}(\boldsymbol{X},\delta)$, $\boldsymbol{r}(\boldsymbol{X})$, $H(\boldsymbol{X})$, $\boldsymbol{g}(\boldsymbol{X},\delta)$ and a desired equilibrium $\boldsymbol{X}^*$, it is possible to define the functions $\delta = \beta(\boldsymbol{X})$, $\boldsymbol{j}_{\boldsymbol{a}}(\boldsymbol{X})$, $\boldsymbol{r}_{\boldsymbol{a}}(\boldsymbol{X})$ and $\boldsymbol{K}(\boldsymbol{X})$ while satisfying the matching equation presented in (5).

$$\begin{aligned}&[\boldsymbol{j}(\boldsymbol{X},\beta(\boldsymbol{X})) + \boldsymbol{j}_{\boldsymbol{a}}(\boldsymbol{X})\\ &- \{\boldsymbol{r}(\boldsymbol{X}) + \boldsymbol{r}_{\boldsymbol{a}}(\boldsymbol{X})\}]\,\boldsymbol{K}(\boldsymbol{X})\\ &= -[\,\boldsymbol{j}_{\boldsymbol{a}}(\boldsymbol{X}) - \boldsymbol{r}_{\boldsymbol{a}}(\boldsymbol{X})]\frac{\partial H}{\partial \boldsymbol{X}} + \boldsymbol{g}(\boldsymbol{X},\beta(\boldsymbol{X}))\end{aligned} \tag{5}$$

Hereby, the subscript $a$ stands for assigned. The matching equation (5) is a Partial Differential Equation (PDE). The assigned interconnection matrix $\boldsymbol{j}_{\boldsymbol{a}}(\boldsymbol{X})$ and the assigned damping matrix $\boldsymbol{r}_{\boldsymbol{a}}(\boldsymbol{X})$ must fulfill the four conditions that are presented in Table I. When the conditions (6)-(9) are satisfied, the resulting closed loop system is PCH, and it exhibits the dynamics described by (4) stabilized around $\boldsymbol{X}^*$.

TABLE I CONDITIONS OF IDA-PBC

| | | |
|---|---|---|
| Structure Preservation | $\boldsymbol{j}_{\underline{d}}(\boldsymbol{X}) = \boldsymbol{j}(\boldsymbol{X},\beta(\boldsymbol{X})) + \boldsymbol{j}_{\boldsymbol{a}}(\boldsymbol{X}) = -\boldsymbol{j}_{\underline{d}}{}^{T}(\boldsymbol{X})$<br>$\boldsymbol{r}_{\underline{d}}(\boldsymbol{X}) = \boldsymbol{r}(\boldsymbol{X}) + \boldsymbol{r}_{\boldsymbol{a}}(\boldsymbol{X}) = \boldsymbol{r}_{\underline{d}}{}^{T}(\boldsymbol{X}) \geq 0$ | (6) |
| Integrability | $\frac{\partial \boldsymbol{K}}{\partial \boldsymbol{X}} = \left(\frac{\partial \boldsymbol{K}}{\partial \boldsymbol{X}}\right)^{T}$ | (7) |
| Equilibrium Assignment | $\frac{\partial H_{\underline{d}}}{\partial \boldsymbol{X}}(\boldsymbol{X}^*) = 0$ | (8) |
| Lyapunov Stability | $\frac{\partial^2 H_{\underline{d}}}{\partial \boldsymbol{X}^2}(\boldsymbol{X}^*) > 0$ | (9) |

To shape the energy of the controller, the assigned energy $H_a$ must be defined as specified in (10).

$$\begin{aligned}&H_a(\boldsymbol{X}) = H_{\underline{d}}(\boldsymbol{X}) - H(\boldsymbol{X})\\ &\frac{\partial H_a}{\partial \boldsymbol{X}} = \boldsymbol{K}(\boldsymbol{X})\end{aligned} \tag{10}$$

Hence, the matching equation in (5) becomes an algebraic equation in terms of $\boldsymbol{j}_{\underline{d}}$ and $\boldsymbol{r}_{\underline{d}}$ [21].

## III. APPLICATION OF IDA-PBC DESIGN ON DAB MODELS

In the following subsections, the design outlined in Section II is applied to the DAB FAM, which is based on PSM and was introduced in [5].

In the FAM, the internal dynamics of the leakage inductance, transformer winding resistance, and the phase shift of the DAB, depicted in Fig. 1, are transferred to the output capacitance of the DAB. This means that they are state space averaging equations of the output capacitor.

The single-phase DAB topology consists of two H-bridges and a medium frequency AC link transformer as shown in Fig. 1. The primary and secondary bridges act as inverter and rectifier, correspondingly. In high power applications, the PSM technique is applied for the synthesis of the gate signals, this results in a phase shifted square wave voltage waveform across the two terminals of the medium frequency transformer. Power flow in the AC link takes place through the leakage inductance of the transformer and it can be controlled by the phase shift $\delta$ [5], [13], [14].

With an abuse of notation, let $\boldsymbol{j}$ be the interconnection matrix for the system presented in Fig. 1. Given that a capacitor is present at the output side, with no further energy storing passive elements, the interconnection matrix is $\boldsymbol{j} = 0$, which fulfills the antisymmetric property. Since $\boldsymbol{j} = 0$, it follows that $\boldsymbol{j}_{\boldsymbol{a}} = 0$ to allow $\boldsymbol{j}_{\underline{d}}$ to be an antisymmetric matrix, in order to satisfy the structure preservation condition (6). Non-zero values of $\boldsymbol{j}_{\boldsymbol{a}}$ would lead to a violation of the antisymmetric property of $\boldsymbol{j}_{\underline{d}}$, which violates the structure preservation condition (6).

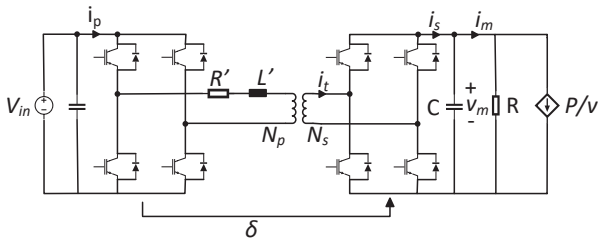


Fig. 1 DAB feeding a CPL

The charge $q$ is typically selected as the energy variable for the capacitor according to the traditional PCH formulation [21], and it is mapped to the energy vector $x$:

$$x = q = Cv \tag{11}$$

The total energy function, which corresponds to the Hamiltonian $H$ of the system depicted in Fig. 1 is:

$$H = \frac{x^2}{2C} \tag{12}$$

This corresponds to the energy stored in the output capacitor. The desired energy function $H_{\underline{d}}$ is selected as follows:

$$H_{\underline{d}} = \frac{(x - x^*)^2}{2C} \tag{13}$$

where $x^*$ is the desired charge setpoint. The selected $H_{\underline{d}}$ satisfies equilibrium assignment condition (8) and Lyapunov stability conditions (9). From equations (10) and (13), $\boldsymbol{K}$ can be defined as shown below:

$$\frac{\partial H_a}{\partial \boldsymbol{X}} = \boldsymbol{K} = -\frac{x^*}{C} \tag{14}$$

Here, $\boldsymbol{K}$ satisfies the integrability condition in (7).

The input matrix $\boldsymbol{g}$ is the input current $i_s$, which is the transferred dynamics of the transformer leakage inductance, transformer winding resistance and phase shift to the output capacitor. $i_s$ is subject to different dynamics according to the different models. The damping matrix $\boldsymbol{r}$ consists of the damping elements present in the system i.e. resistances, CPLs and the transferred transformer winding resistance. The assigned damping parameter $r_1$ is the one and only control design parameter. This method shows that the IDA-PBC

design can be simplified to rearranging the state space equations of the DAB to match the PCH form.

The IDA-PBC control law in accordance to the DAB FAM is detailed the following subsection.

### A. Fundamental Averaged Model (FAM) IDA-PBC

The average fundamental power transfer in the DAB, while using the first order state space averaged model is described by (15) [5]; where $n_t$ is the secondary to primary turns ratio of the transformer and $L'$ corresponds to the equivalent transformer inductance referred to the primary side.

$$P_t = \frac{V_{in}\, v\, \delta}{n_t \omega L'}\left(1-\frac{\delta}{\pi}\right) \tag{15}$$

This model does not consider winding power losses due to $R'$ and the power transferred through higher order odd harmonics. From the power balance equation, the secondary side DC current is given by (16).

$$P_t = i_s v \rightarrow i_s = \frac{V_{in}\,\delta}{n_t \omega L'}\left(1-\frac{\delta}{\pi}\right) \tag{16}$$

Applying the KCL at the output node and using (16), the non-linear state space equation of the DAB can be written as:

$$C\frac{dv}{dt} = -\frac{v}{R} - \frac{P}{v} + \frac{V_{in}\,\delta}{n_t \omega L'}\left(1-\frac{\delta}{\pi}\right) \tag{17}$$

Substituting the energy vector of (11) in (17) leads to:

$$\frac{dx}{dt} = -\left(\frac{1}{R}+\frac{PC^2}{x^2}\right)\left(\frac{x}{C}\right) + \frac{V_{in}\,\delta}{n_t \omega L'}\left(1-\frac{\delta}{\pi}\right) \tag{18}$$

It is possible to do the following mapping when comparing the PCH formulation in (1) with (18):

$$\boldsymbol{X} = x \quad \boldsymbol{j} = 0 \quad \boldsymbol{r} = \left(\frac{1}{R}+\frac{PC^2}{x^2}\right) \quad \boldsymbol{g} = \frac{V_{in}\,\delta}{n_t \omega L'}\left(1-\frac{\delta}{\pi}\right) \tag{19}$$

Assigning $\boldsymbol{r_a} = r_1$, where $r_1$ is a positive constant to inject additional damping, modifies the overall damping matrix of the system. In accordance with (6), the overall damping can be written as:

$$\boldsymbol{r_{\underline{d}}} = r_1 + \boldsymbol{r} = r_1 + \left(\frac{1}{R}+\frac{PC^2}{x^2}\right) \tag{20}$$

Substituting $\boldsymbol{j}$, $\boldsymbol{j_a}$, $\boldsymbol{r}$, $\boldsymbol{r_a}$, $\boldsymbol{K}$, $\boldsymbol{g}$ and $H$ in the matching equation (5) enables us to derive the control law $\delta$, where the subscript $m$ refers to measured values, while * denotes the reference.

$$\delta = \frac{\pi}{2} - \sqrt{\left(\frac{\pi}{2}\right)^2 - \left(\frac{\pi n_t \omega\, L' i_m v^*}{V_{in}\, v_m}\right) + \left(\frac{\pi n_t \omega L'}{V_{in}}\right) r_1 (v_m - v^*)} \tag{21}$$

Equation (21) is the resulting IDA-PBC for the FAM of the DAB. In practice, the voltage is measured instead of the capacitor charge. Furthermore, $i_m$ is the current measurement after the filter capacitor, $v_m$ denotes the measured output voltage, and $v^*$ is the desired reference bus voltage.

As depicted in Fig. 2, higher values of $r_1$ can reduce the steady state output voltage error and improve the transient performance of the controller, at the cost of an increased ripple.

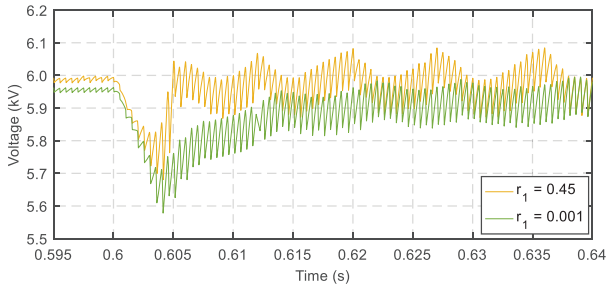


Fig. 2 HiL Results *5MW* DAB submodule - variations of $r_1$

To quantify the effect of the control parameter $r_1$ on the eigenvalues, we consider the closed loop PCH dynamics (4) and the control law from (21) in the following subsection.

### B. Eigenvalues of Fundamental Averaged Model (FAM)

Equation (21) is the algebraic IDA-PBC of the DAB. The closed loop expression is obtained by inserting (21) in equation (4):

$$\frac{dx}{dt} = -\left(r_1+\frac{1}{R}\right)\left(\frac{x}{C}\right) - \frac{PC}{x} + \frac{PC^2}{x^2}\frac{x^*}{C} + \left(r_1+\frac{1}{R}\right)\frac{x^*}{C} \tag{22}$$

Linearizing equation (22) around equilibrium point $x^*$ for small signal stability analysis, leads to (23), where $\Delta x$ is the small perturbation around equilibrium point.

$$\frac{d\Delta x}{dt} = -\left\{\left(r_1+\frac{1}{R}\right)\frac{1}{C} + \frac{PC}{x^{*2}}\right\}\Delta x \tag{23}$$

The eigenvalue of the closed loop system is defined as:

$$\lambda = -\left\{\left(r_1+\frac{1}{R}\right)\frac{1}{C} + \frac{PC}{x^{*2}}\right\}. \tag{24}$$

### C. Limits of Control Parameter $r_1$

Due to the structure preservation condition of the IDA-PBC design (6), the damping injection parameter $r_1$ must be positive semidefinite, which translates into the following lower bound $r_1 \geq 0$.

From Fig. 3, we observe that the system is stable for any positive damping injection $r_1$.

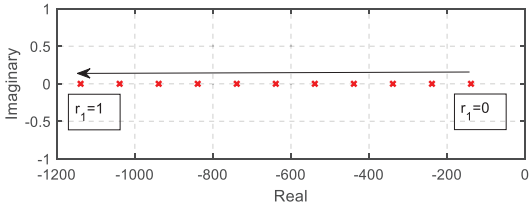


Fig. 3 Root Locus Plot for FAM Eigenvalues

Since increasing the damping injection would theoretically increase the passivity of the closed loop system, selecting an arbitrarily large value for $r_1$ would be desirable. However, the selection of the value for $r_1$ must comply with the maximally reachable dynamics of the system, which depend on the switching frequency, installed capacitance and load.

In order to derive an upper bound for $r_1$, we start from the power transfer equation for the DAB, which is modelled as a current source according to (16). Since (16) is obtained by state space averaging, it is only valid inside the frequency range in which the DAB operates, where the average power values are calculated over one switching cycle $T_s = \frac{1}{f_s}$. The

This article has been accepted for publication in a future issue of this journal, but has not been fully edited. Content may change prior to final publication. Citation information: DOI 10.1109/TIE.2019.2901645, IEEE Transactions on Industrial Electronics



validity of the model determines where the poles of the plant can be moved by the controller. From (24) and assuming that the model is valid up to the switching period, with $f_s = 1kHz$ and $x = Cv$, a pole placement is possible up to:

$$\lambda = -2\pi f_s \approx -6.2832e + 03. \quad (25)$$

Solving equation (26) according to the parameters in Table II and considering, e.g. $R = 18\Omega$ and $P = 1MW$, an upper bound for $r_1$ is obtained, $r_1 \leq 3.05$.

$$r_1 \leq -\lambda C - \frac{1}{R} - \frac{P}{V^2} \quad (26)$$

In the state space averaged modelling approach, the converter behavior is studied at frequencies well below the Nyquist rate i.e. $0.5f_s$, which would lead to an upper bound of $r_{1-0.5f_s} \leq 1.48$.

Further restrictions can be used to define the upper bound of $r_1$ depending on the frequency for which the state space averaged model provides an accurate representation, given a certain switching frequency. This is around one decade less than the switching frequency, which leads to an upper bound of $r_{1-0.1f_s} \leq 0.23$.

To understand if the control performance could be improved by including the transformer resistance and the contribution of higher order harmonic components, we performed further analyses considering the harmonic modelling approach presented in [15], which transfers the AC link dynamics to the output DC port. As an outcome, no substantial improvement in performance could be obtained that would justify the increased complexity of the harmonic modelling in comparison with the FAM.

## IV. Circuit Representation of IDA-PBC

IDA-PBC modifies the energy dissipation of the system through injection of virtual resistances to damp the system oscillations and to ensure the closed loop system to be passive. In this part, we present a circuit analogy of the virtual damping component and where it is located. The authors in [24] explained in detail how the soft switching boundary conditions are impacted by a) modulation strategy used in primary and secondary bridges b) operational input and output DC voltages and c) the admittance matrix of the AC link.

If the virtual damping element would be located inside the AC link, then the admittance matrix would be influenced by the control law, which in turn would impact the soft switching boundary. From reference [25], the virtual equivalent circuit dynamics for the closed loop system are described by the right hand side of matching equation (5).

$$\frac{dX}{dt} = -[j_a - r_a]\frac{\partial H}{\partial X} + g \quad (27)$$

Applying the FAM of the DAB in (27), the closed loop equation is obtained to study the virtual circuit.

$$\frac{dX}{dt} = -\left\{\left(r_1 + \frac{1}{R}\right)\frac{1}{C} + \frac{PC}{x^{*2}}\right\}\left(\frac{x - x^*}{C}\right) \quad (28)$$

Substituting (11) in (28) and simplifying leads us to (29), where the terms are rearranged and classified based on their presence in the real circuit (black color) or the virtual circuit (red color).

$$C\frac{dv}{dt} = \overbrace{-r_1 v}^{R_{damp}^{-1}} - \frac{v}{R} - \frac{P}{v} + \overbrace{\left(r_1 + \frac{1}{R}\right)v^*}^{I_{s2}} + \overbrace{\frac{Pv^*}{v^2}}^{I_{s1}} \quad (29)$$

The term $\frac{Pv^*}{v^2}$ corresponds to a Voltage Controlled Current Source (VCCS) $I_{s1}(v)$ that compensates for the non-linear effects of the CPL. The term $(r_1 + R^{-1})v^*$ is a Constant Current Source (CCS) denoted by $I_{s2}$ that compensates for linear loads. Additionally, due to the injected damping by the tuning parameter $r_1$, an additional positive damping resistor $R_{damp} = r_1^{-1}$ is present. The virtual equivalent circuit with the above-mentioned components is shown in Fig. 4. One can observe that the CCS $I_{s2}$ and the damping resistor $R_{damp}$ lie on the secondary DC side; therefore, they do not affect the soft switching boundaries [24].

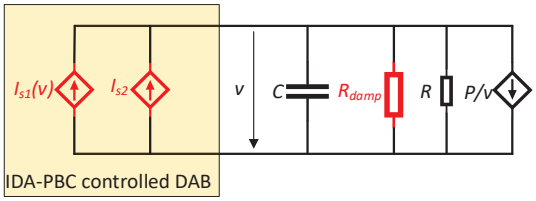


Fig. 4 Virtual equivalent circuit

## V. Hardware in the Loop (HiL) Experiments

This section provides the Microgrid description, the HiL setup and the proof of feasibility for the IDA-PBC control approach via HiL experiments.

### A. Microgrid and System Level Control Description

Fig. 5 depicts the radial structure of the DAB based Microgrid. Each of the three DC renewable sources is connected to a Line Regulating Converter (LRC), denoted by a constant voltage source of *9kV*. Each LRC consists of four DAB submodules of *5MW*. The submodule is depicted in Fig. 1, with its parameters shown in Table II. The submodules are connected in parallel configuration on the input and output side for load sharing [11].

TABLE II DAB Module Parameters

| $V_{in}$ | $v^*$ | $f_s$ | $L'$ | $R'$ | $n_t$ |
|---|---|---|---|---|---|
| 9 kV | 6 kV | 1 kHz | 1.518 mH | 0.325 Ω | 2/3 |

Thus, each LRC is rated at *20MW* leading to a total generation capacity of *60MW*. A CLC π-filter is placed at the output of each LRC to prevent circulating currents. The filter parameters are provided in Table III, where $C_o$ denotes the LRC side capacitance and $C_g$ is the MVDC bus facing capacitance. A power sharing ratio of *4:3:3* is enforced between $LRC_1$:$LRC_2$:$LRC_3$. The loads are lumped into an equivalent tightly regulated POL converter, which steps down the voltage from *6kV* to *3kV* and acts as CPL.

The parameters of the POL are described in Table IV. An LC filter is used at the input side of the POL converter to mitigate line current harmonics. $L_s$ and $C_s$ are the input LC filter parameters and $L_n$ and $C_n$ are the output filter parameters. The proportional and integral control gains for the POL are $K_{pL}$ and $K_{iL}$ respectively.

This article has been accepted for publication in a future issue of this journal, but has not been fully edited. Content may change prior to final publication. Citation information: DOI 10.1109/TIE.2019.2901645, IEEE Transactions on Industrial Electronics



TABLE III PI FILTER PARAMETERS

| $C_o = 4C$ | $L_f$ | $R_f$ | $C_g$ |
|---|---|---|---|
| 2 mF | 500µH | 0.06 Ω | 262 µF |

TABLE IV PARAMETERS OF POL

| $f_s$ | $C_n$ | $L_n$ | $C_s$ | $L_s$ | $R_s$ | $K_{pL}$ | $K_{iL}$ |
|---|---|---|---|---|---|---|---|
| 3 kHz | 34 µF | 12.5 mH | 1.5 mF | 300 µH | 0.01 Ω | 1.2 e-3 | 4.066 e-2 |

Fig. 6 depicts the two control loops used inside the MVDC Microgrid. A central PI controller acts as the secondary controller using droop logic for power sharing, with control parameters $K_{ps} = 0.5$ and $K_{is} = 200$. The primary control is the IDA-PBC control law.

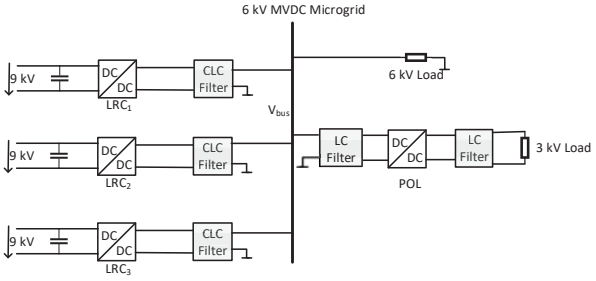


Fig. 5 MVDC Microgrid

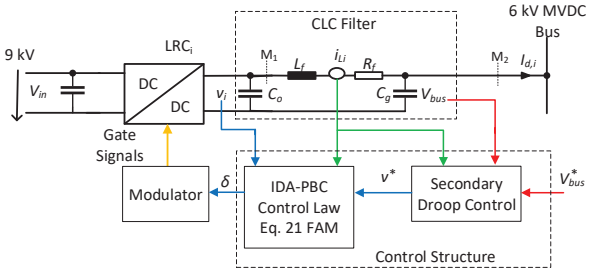


Fig. 6 Proposed control approach

## B. HiL Setup

The HiL setup consists of an OPAL-RT real time simulator, where the MVDC grid described in the previous subsection and depicted in Fig. 5 is implemented.

The full switched models of the DAB converter based MVDC Microgrid are implemented in OPAL-RT. Primary and secondary bridges of the DAB are realized through IGBT Diode models. A dead time delay of *7µs* is implemented based on the data sheet of *ABB 5SNA 0750G650300* IGBTs. A linear transformer model is used in the AC link. Three digitally controlled switching-type DABs, each consisting of four submodules, are connected to a common DC bus.

At the DC bus a resistive load and a switching-type buck-converter acting as a CPL is implemented. The execution time of the MVDC grid in OPAL-RT simulator is *1µs*. The modulation block for the gate signal generation is implemented within OPAL-RT. OPAL-RT is interfaced to a real time host PC with an NI PCIe-7841R Card, which holds the Virtex-5 FPGA. The data acquisition and the IDA-PBC control of each LRC is implemented in an individual FPGA Target. The FPGA is programmed with the National Instruments Real Time Target. The measurements and control calculations are updated with a sampling time of *10µs*. Six analog channels are used as inputs to receive the voltage and current measurements and 3 analog channels are used to update the phase shifts. The measured current, at the point $M_2$, and bus voltage are filtered by a first order low pass Butterworth filter with a cutoff frequency of *2500 rad/s*.

## C. HiL Results

HiL experiments show the effectiveness of the IDA-PBC based control design against large disturbances in DC Microgrids. An initial base load of *10MW* resistive load and a POL of *21MW* is considered. The controller is evaluated with $r_1 = 0.3$.

### 1) Load Step-up

Fig. 7, Fig. 8 and Fig. 9 depict the HiL results for load step up for the voltages, currents and phase shift, respectively. The POL power is increased from *21MW* to *32MW* at *t=0.5s*. Due to the load step up, the MVDC bus voltage decreases and currents supplied by LRC increase to support the higher load demand. From Fig. 8, all LRCs share the load current according to predefined power-sharing proportions.

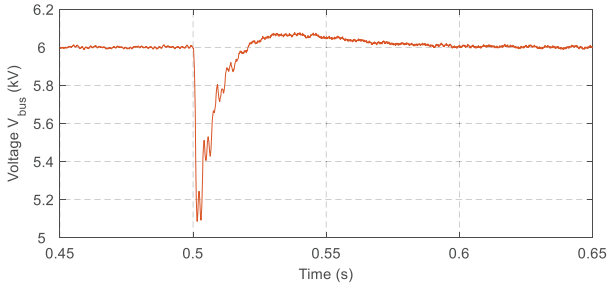


Fig. 7 HiL results for load step up – voltages

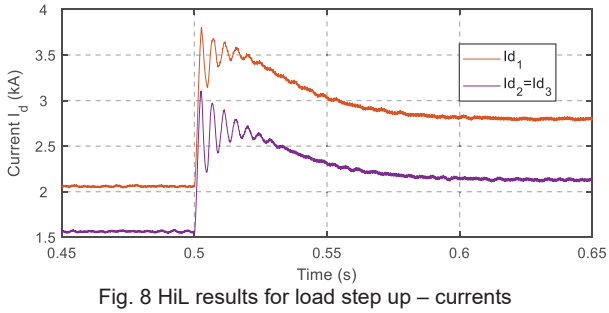


Fig. 8 HiL results for load step up – currents

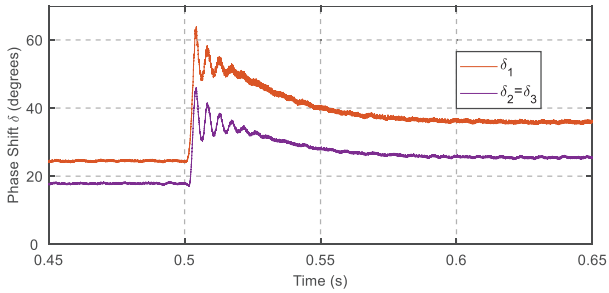


Fig. 9 HiL results for load step up – phase shifts

### 2) Converter Disconnection

The POL power is *21MW* and the LRC-3 is disconnected. In Fig. 11, the supplied current $I_{d3}$ decreases to zero with some oscillation due to which $I_{d3}$ goes negative. However, due to the presence of CLC filter, the secondary side DC current of

This article has been accepted for publication in a future issue of this journal, but has not been fully edited. Content may change prior to final publication. Citation information: DOI 10.1109/TIE.2019.2901645, IEEE Transactions on Industrial Electronics



the LRC is positive. In Fig. 10, the voltage drop is compensated by the other LRCs.

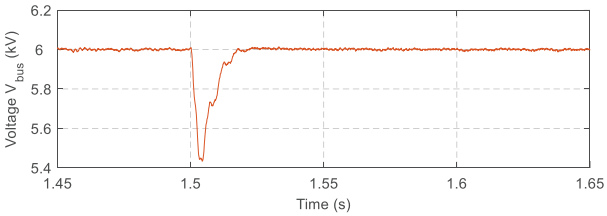


Fig. 10 HiL results for converter disconnection (LRC-3) – voltages

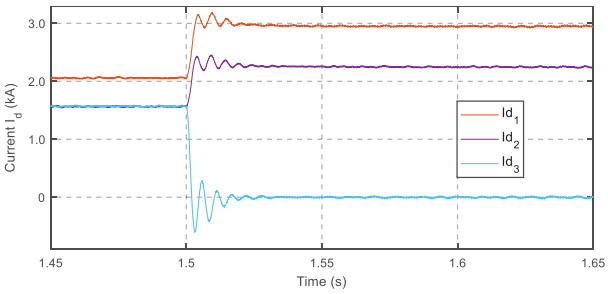


Fig. 11 HiL results for converter disconnection (LRC-3) – currents

### 3) *Input Voltage Fluctuation*

The input side of the LRC could be a collector grid of a large PV park as illustrated in [2]. In such a scenario, due to sudden changes e.g. cloud covering, a voltage drop of *10%* occurs. By enforcing an input voltage drop from *9kV* to *8.1kV* in all converters at *t=0.7s*. The total load is *42MW*. This results in a maximum under voltage of *0.2kV*. The grid voltage is back at the reference value in less than *15ms*.

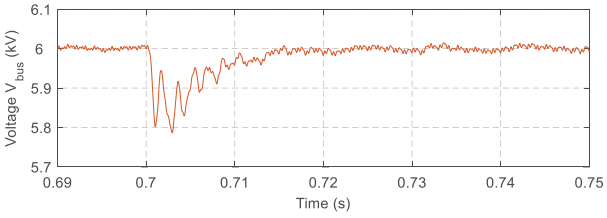


Fig. 12 HiL results for Input voltage fluctuation – voltages

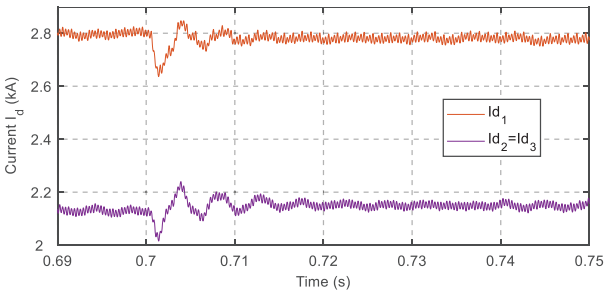


Fig. 13 HiL results for Input voltage fluctuation – currents

## VI. Low Power Prototype

The experimental setup used for the validation of the proposed IDA-PBC control technique is presented in Fig. 14. This reflects a standalone DAB interfaced via an output capacitor to a load. For the primary and secondary bridges, *3L SKiiP 28 MLI 07E3V1* evaluation inverters from Semikron are used respectively. The IDA-PBC algorithm is loaded into the FPGA target of the control platform.

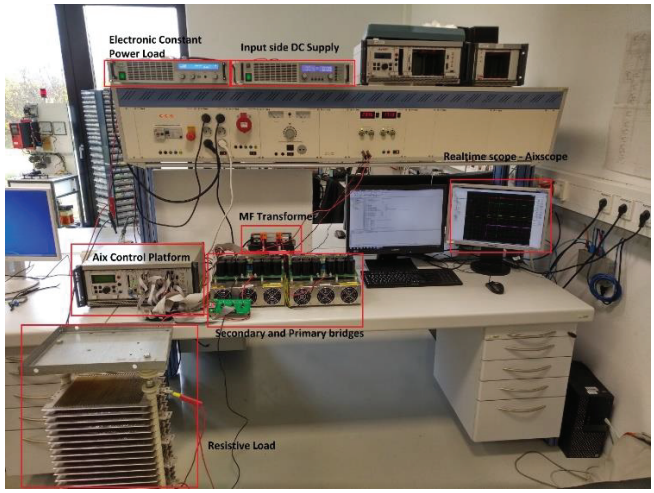


Fig. 14 Low power prototype – experimental setup

A medium frequency transformer rated at *1kHz* for *400V* and *3A* is used to serve as the AC link transformer of the DAB. The turns ratio of the transformer is *1:1*.

At the load side, a constant resistive load is used in parallel with an electronic load operated in constant power mode.

The experimental evaluation takes places at point $M_1$ of Fig. 6 without the additional LC component and the secondary PI-droop controller. The parameters of the low power prototype experiments are summarized in Table V.

The primary and secondary DC voltage are measured along with the load current. The IDA-PBC control law based on FAM model is used to calculate the phase shift, which is updated at a rate of *1kHz*.

TABLE V LOW POWER PROTOTYPE

| $V_{in}$ | $v^*$ | $f_s$ | $L'$ | $R'$ | $n_t$ | $R_{res}$ |
|---|---|---|---|---|---|---|
| 100 V | 100V | 1 kHz | 440 µH | 0.3 Ω | 1:1 | 63 Ω |

Initially, a resistive load of *63Ω* is connected on the secondary DC side. A load step up and step down of *100W* was programmed through an electronic constant power load. The above experiment was repeated for different values of $r_1$. When the load step up occurs, the current under goes a sudden ramp change and the controller reacts by increasing the phase shift in order to regulate the output voltage of *100V*. The controller is able to stabilize the DC bus for various values of the tuning parameter $r_1$ inside the interval [*0.1-1*]. Satisfactory load voltage regulation was observed in all test cases. Although it should be highlighted that the steady state error in the output voltage in Fig. 15 is consistent with the observations of Fig. 2.

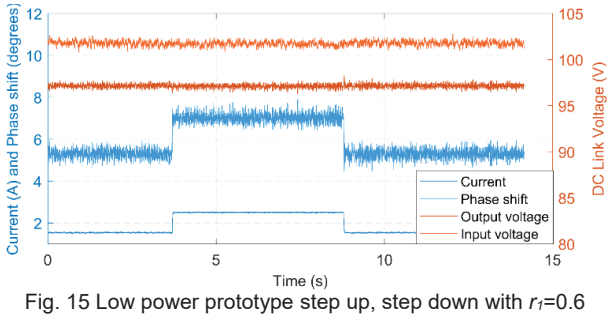


Fig. 15 Low power prototype step up, step down with $r_1$=0.6

This article has been accepted for publication in a future issue of this journal, but has not been fully edited. Content may change prior to final publication. Citation information: DOI 10.1109/TIE.2019.2901645, IEEE Transactions on Industrial Electronics



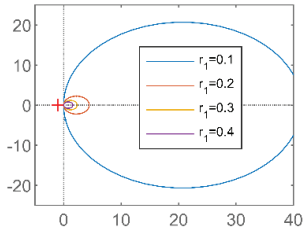


Fig. 16 Closed Loop Nyquist plot at $M_1$

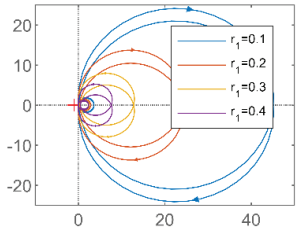


Fig. 17 Closed Loop Nyquist plot at $M_2$

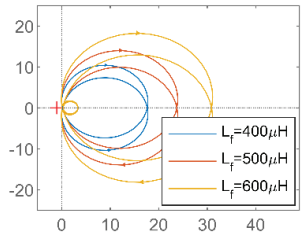


Fig. 18 Closed Loop Influences of on $L_f$

## VII. Passivity Analysis and Region of Attraction

In this section, we perform two analyses supporting the previous HiL experiments, which are based on the MVDC Microgrid setup depicted in Fig. 6.

The closed loop output impedance of the DAB under IDA-PBC, law is computed at the point $M_1$, is depicted in Fig. 16. It can be observed that the passivity increases while increasing $r_1$. Fig. 17 depicts the closed loop output impedance, computed at the point $M_2$, which includes the effects of the Secondary PI-Droop Control. This output impedance represents one complete source branch.

A variation in $r_1$ was performed and the Nyquist plots show that the complete system is passive and stable. In Fig. 18, a further variation of the branch with respect to varying inductances was performed and it highlights the passivity-by-design property of the PCH+IDA-PBC approach. Parallelizing those branches and connecting them to a common DC bus does not interfere with the passivity property, as parallel connection of PCH systems forms again a PCH system.

The passivity property is further verified experimentally through HiL. A similar setup as described in [6] is used, where a sinusoidal perturbation current source is connected in shunt at node $M_2$. The amplitude of the perturbation is fixed as 10% of load current. A load of *10MW* and $r_1$*=0.3* are considered. A single frequency sweep from *20Hz* to *5kHz* is conducted.

The perturbation current flowing into the LRC converter and the grid capacitor voltage is recorded and post processed in real time based on the Recursive Fourier Transform algorithm [6].

The impedance obtained from the HiL experiment satisfies both the low and high frequency behavior predicted by the analytical model as presented in Fig. 19 and Fig. 20.

The resonance peak obtained in the HiL simulation occurs at *~450Hz* compared to *~570Hz* in the analytical model. It is slightly shifted owing to the dead-time delays and other computational delays which are considered in the HiL experiments. Additionally, the internal resistance of the transformer winding is not considered in the control law derivation based on FAM, therefore, a minor difference in the resonance peak is observed when measured through the HiL setup. For a passive system, the phase must strictly lie between *-90* to *+90* degrees. It can be appreciated that the measured phase of the impedance from HiL experiment fulfills the passivity condition as predicted by the analytical model.

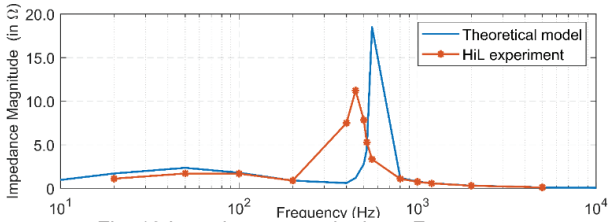


Fig. 19 Impedance magnitude vs Frequency

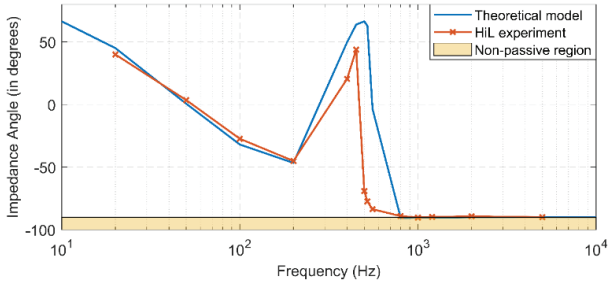


Fig. 20 Impedance angle vs Frequency

To enhance the small signal passivity analysis of the system, a large signal analysis is performed to estimate the Region of Attraction (ROA). In Fig. 21, an equilibrium point is marked with the blue asterisk. On the y-axis the bus voltage at $C_g$ is given, the x-axis represents the inductor current while the voltage over output capacitor $C_o$ of the DAB is represented on the z-axis. The direction of the cones indicates the movements of the states in the phase-space, which points towards the center equilibrium point, and hence indicates large signal stability.

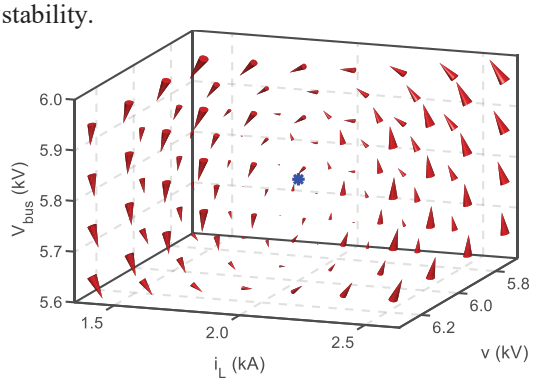


Fig. 21 Cone-plot of the non-linear LRC model showing global convergence

## VIII. Conclusions

This paper presented the PCH modelling based on the FAM, as well as, the IDA-PBC control of DAB converters in DC Microgrid applications. The presented FAM IDA-PBC is a passivity-by-design approach that requires only local measurements for control synthesis; thanks to the passivity

property, the interconnection of IDA-PBC controlled DABs and passive components results on a system that is passive and stable under large signal disturbances.

Contrary to previous approaches [18], the proposed IDA-PBC considers PSM, which enables high power applications due to significantly lower switching losses and does not alter the soft switching boundaries.

The IDA-PBC approach reduces the requirement on complex modelling techniques from a system level perspective and requires the tuning of a single control parameter $r_1$, for which we provided practical limits based on the local passive components, the switching frequency and the load.

Via HiL experiments, we evaluated the effectiveness of the proposed approach against load and input variations and achieved voltage stability under large signal disturbances; moreover, we validated the passivity property considering the limits of the control parameter $r_1$.

The results obtained from the low power prototype, proved the feasibility of the proposed approach. Hence, the proposed approach is suitable for real-time and closed loop control of DAB based Microgrids.

Future work would be firstly to determine a generalization for tuning control parameters and their corresponding limits given different converter topologies; secondly, to investigate if the integral action on each local IDA-PBC controller would be better suited than the secondary droop PI for steady state error removal.

## APPENDIX

This appendix provides the equations and summarizes the steps required for estimating the ROA. The following state space equations characterize the system depicted in Fig. 6 where δ is the corresponding control law.

$$C_o \frac{dv}{dt} = \frac{4\, V_{in}\, \delta}{n_t \omega L'}\left(1 - \frac{\delta}{\pi}\right) - i_L \tag{30}$$

$$L_f \frac{di_L}{dt} = v - V_{bus} - i_L R_f \tag{31}$$

$$C_g \frac{dV_{bus}}{dt} = i_L + I_d \tag{32}$$

$$\frac{dx_{bus}}{dt} = V_{bus}^* - V_{bus} \tag{33}$$

The bus voltage reference provided by the secondary to primary controller is given by:

$$v^* = K_{pd}(V_{bus}^* - V_{bus}) + K_{id} x_{bus} - i_L R_{droop} \tag{34}$$

This leads to the non-linear system of equations in the form of:

$$\frac{dX_{LRC}}{dt} = f_{LRC}(X_{LRC}, I_d) \tag{35}$$

Where $X_{LRC}$ consists of the state vector $X_{LRC} = [v\ i_L\ V_{bus}\ x_{bus}]^T$.

## ACKNOWLEDGMENT

The authors would like to thank Lisette Joanne Cupelli for various helpful discussions that improved the content and the presentation of the paper and to thank Nisar Ahmed Khan for his help with the experimental setup.

## REFERENCES

[1] M. Stieneker, Nurhan Rizqy Averous, N. Soltau, H. Stagge and R. W. De Doncker, "Analysis of wind turbines connected to medium-voltage DC grids," *2014 16th European Conference on Power Electronics and Applications*, Lappeenranta, 2014, pp. 1-10.

[2] H. A. B. Siddique and R. W. De Doncker, "Evaluation of DC Collector-Grid Configurations for Large Photovoltaic Parks," in *IEEE Transactions on Power Delivery*, vol. 33, no. 1, pp. 311-320, Feb. 2018.

[3] U. Javaid, F. D. Freijedo, D. Dujic and W. van der Merwe, "Dynamic Assessment of Source–Load Interactions in Marine MVDC Distribution," in *IEEE Transactions on Industrial Electronics*, vol. 64, no. 6, pp. 4372-4381, June 2017.

[4] M. Cupelli *et al*., "Power Flow Control and Network Stability in an All-Electric Ship," in *Proceedings of the IEEE*, vol. 103, no. 12, pp. 2355-2380, Dec. 2015.

[5] R. W. De Doncker, D. M. Divan, M. H. Kheraluwala. "A three-phase softswitched high-power-density DC/DC converter for high-power applications". In: *IEEE Transactions on Industry Applications*. 1991.

[6] F. D. Freijedo, E. R. Diaz and D. Dujic, "Stable and Passive High-Power Dual Active Bridge Converters Interfacing MVDC Grids," in *IEEE Transactions on Industrial Electronics*.

[7] N. Vafamand, M. H. Khooban, T. Dragicevic and F. Blaabjerg, "Networked Fuzzy Predictive Control of Power Buffers for Dynamic Stabilization of DC Microgrids," in *IEEE Transactions on Industrial Electronics*.

[8] T. Dragičević, X. Lu, J. C. Vasquez and J. M. Guerrero, "DC Microgrids—Part I: A Review of Control Strategies and Stabilization Techniques," in *IEEE Transactions on Power Electronics*, vol. 31, no. 7, pp. 4876-4891, July 2016.

[9] M. Cupelli, L. Zhu and A. Monti, "Why Ideal Constant Power Loads Are Not the Worst Case Condition From a Control Standpoint," in *IEEE Transactions on Smart Grid*, vol. 6, no. 6, pp. 2596-2606, Nov. 2015.

[10] N. Doerry, "Naval Power Systems: Integrated power systems for the continuity of the electrical power supply.," in *IEEE Electrification Magazine*, vol. 3, no. 2, pp. 12-21, June 2015.

[11] M. Cupelli, S. K. Gurumurthy and A. Monti, "Modelling and control of single phase DAB based MVDC shipboard power system," *IECON 2017 - 43rd Annual Conference of the IEEE Industrial Electronics Society*, Beijing, 2017, pp. 6813-6819.

[12] S. P. Engel, N. Soltau, H. Stagge and R. W. De Doncker, "Dynamic and Balanced Control of Three-Phase High-Power Dual-Active Bridge DC–DC Converters in DC-Grid Applications," in *IEEE Transactions on Power Electronics*, vol. 28, no. 4, pp. 1880-1889,

[13] H. Qin and J. W. Kimball, "Generalized average modeling of dual active bridge DC–DC converter," *IEEE Trans. Power Electron.*, vol. 27, no. 4, pp. 2078–2084, Apr. 2012.

[14] D. S. Segaran, "Dynamic modelling and control of dual active bridge Bi-directional DC–DC converters for smart grid applications," Ph.D. dissertation, RMIT Univ., Melbourne, VIC, Australia, 2013.

[15] E. De Din, H. A. B. Siddique, M. Cupelli, A. Monti and R. W. De Doncker, "Voltage Control of Parallel-Connected Dual-Active Bridge Converters for Shipboard Applications," in *IEEE Journal of Emerging and Selected Topics in Power Electronics*, vol. 6, no. 2, pp. 664-673, June 2018.

[16] A. Kwasinski and P. T. Krein, "Stabilization of constant power loads in Dc-Dc converters using passivity-based control," *INTELEC 07 - 29th International Telecommunications Energy Conference*, Rome, 2007, pp. 867-874.

[17] M. Cupelli, S. K. Bhanderi, S. K. Gurumurthy and A. Monti, "Voltage control for buck converter based MVDC microgrids with interconnection and damping assignment passivity based control," *2018 19th IEEE Mediterranean Electrotechnical Conference (MELECON)*, Marrakech, 2018, pp. 14-19.

[18] R. V. Meshram, M. Bhagwat, S. Khade, S. R. Wagh, A. M. Stanković and N. M. Singh, "Port-Controlled Phasor Hamiltonian Modeling and IDA-PBC Control of Solid-State Transformer," in *IEEE Transactions on Control Systems Technology*.

[19] G. Bergna-Diaz, D. Zonetti, S. Sanchez, E. Tedeschi and R. Ortega, "PI passivity-based control of modular multilevel converters for multi-terminal HVDC systems," *2017 IEEE 18th Workshop on Control and Modeling for Power Electronics (COMPEL)*, Stanford, CA, 2017, pp. 1-8.

[20] W. He, C.A. Soriano-Rangel, R. Ortega, A. Astolfi, F. Mancilla-David, S. Li, Energy shaping control for buck–boost converters with unknown constant power load, *Control Engineering Practice*, Volume 74, 2018, Pages 33-43

[21] R. Ortega; E. Garcia-Canseco," Interconnection and Damping Assignment Passivity-Based Control: A Survey" European Journal of Control, vol.10, pp.432–450, 2004

[22] IEEE Recommended Practice for 1 kV to 35 kV Medium-Voltage DC Power Systems on Ships," in *IEEE Std 1709-2010*, pp.1-54, 2 Nov. 2010

[23] IEEE Recommended Practice for the Design and Application of Power Electronics in Electrical Power Systems," in *IEEE Std 1662-2016 (Revision of IEEE Std 1662-2008)* , vol., no., pp.1-68, 9 March 2017

[24] J. Riedel, D. G. Holmes, B. McGrath and C. Teixeira, "Maintaining Continuous ZVS Operation of a Dual Active Bridge by Reduced Coupling Transformers," in *IEEE Transactions on Industrial Electronics*.

[25] A. Emadi, A. Khaligh, C. H. Rivetta, G. A. Williamson, "Constant power loads and negative impedance instability in automotive systems: Definition modeling stability and control of power electronic converters and motor drives", *IEEE Trans. Veh. Technol.*, vol. 55, no. 4, pp. 1112-1125, Jul. 2006.

[26] A. Riccobono *et al*., "Stability of Shipboard DC Power Distribution: Online Impedance-Based Systems Methods," in *IEEE Electrification Magazine*, vol. 5, no. 3, pp. 55-67, Sept. 2017.

[27] J. Zeng, Z. Zhang and W. Qiao, "An Interconnection and Damping Assignment Passivity-Based Controller for a DC–DC Boost Converter With a Constant Power Load," in *IEEE Transactions on Industry Applications*, vol. 50, no. 4, pp. 2314-2322, July-Aug. 2014.

[28] E. Hossain, R. Perez, A. Nasiri and S. Padmanaban, "A Comprehensive Review on Constant Power Loads Compensation Techniques," in *IEEE Access*, vol. 6, pp. 33285-33305, 2018.

[29] F. Paz and M. Ordonez, "High-Accuracy Impedance Detection to Improve Transient Stability in Microgrids," in *IEEE Transactions on Industrial Electronics*, vol. 64, no. 10, pp. 8167-8176, Oct. 2017.

**Sriram K. Gurumurthy** (S'18) received the M.Sc. degree in electrical power engineering from RWTH Aachen University, Aachen, Germany in 2017. He is currently a Research Associate with the Institute for Automation of Complex Power Systems, E.ON Energy Research Center, RWTH Aachen University. His research interests include modelling, control, stability analysis and automation of power electronics driven power systems.

**Marco Cupelli** (S'10-SM'16) received the Diploma degree in electrical engineering and business administration from the Technische Universität Darmstadt, Darmstadt, Germany, and the Doctoral degree in electrical engineering from RWTH Aachen University, Aachen, Germany. He is currently the Division Head of power systems control and automation with the E.ON Energy Research Center, RWTH Aachen University, Aachen, Germany. His current research interests include power system control and automation, developing innovative control strategies for medium and low voltage distribution networks and integrating smart metering devices to enable cloud automation solutions.

**Siddharth K. Bhanderi** received the B.Tech. degree in Electrical and Electronics Engineering from National Institute of Technology, Calicut, India, in 2012 and the M.Tech. degree from Indian Institute of Technology (Banaras Hindu University), Varanasi, India in 2014. He is currently pursuing a M.Sc in Electrical Power Engineering at RWTH Aachen University, Germany.

**Antonello Monti** (M'94-SM'02) received the M.Sc. (summa cum laude) and Ph.D. degrees in electrical engineering from the Politecnico di Milano, Milan, Italy, in 1989 and 1994, respectively. He started his career in Ansaldo Industria, Milan, and then moved to the Politecnico di Milano, in 1995, as an Assistant Professor. In 2000, he joined the Department of Electrical Engineering, University of South Carolina, Columbia, SC, USA, as an Associate Professor and then a Full Professor. Since 2008, he has been the Director of the E.ON Energy Research Center, Institute for Automation of Complex Power System, RWTH Aachen University, Aachen, Germany. He has authored or co-authored more than 300 peer-reviewed papers published in international journals and in the proceedings of international conferences. Dr. Monti is a member of the Editorial Board of Sustainable Energy, Grids and Networks (Elsevier) and the Founding Board of Energy Informatics (Springer). He was a recipient of the 2017 IEEE Innovation in Societal Infrastructure Award. He is currently an Associate Editor of the IEEE SYSTEMSJOURNAL and the IEEE Electrification Magazine.

**Philipp Joebges** (S'16) received the B.S. degree and M.Sc. degree from RWTH Aachen University, Aachen, Germany, in 2013 and 2016, respectively, both in electrical engineering. In 2016, he joined the Institute for Power Generation and Storage Systems, E.ON Energy Research Center, RWTH Aachen University, Germany, as a research associate. He became a group leader of the power electronics group in 2018. His research interests include control and real-time simulations of high power converters for medium-voltage dc grids.

**Zhiqing Yang** (S´16) received the B.S. degree from Southwest Jiaotong University, Chengdu, China, and M.S. degree from RWTH Aachen University, Aachen, Germany, in 2013 and 2017, respectively, both in electrical engineering. In 2017, he joined in the Institute for Power Generation and Storage System, E.ON Energy Research Center, RWTH Aachen University, Germany, as a research associate. His research interests include modeling and control of power electronic system with a focus on renewable energy applications.

**Rik W. De Doncker** (F'01) received the Ph.D. degree in electrical engineering from the Katholieke Universiteit Leuven, Leuven, Belgium, in 1986. In 1987, he was appointed as a Visiting Associate Professor at the University of Wisconsin, Madison. After a short stay as an Adjunct Researcher with Interuniversity Microelectronics Centre, Leuven, he joined, in 1989, the Corporate Research and Development Center, General Electric Company, Schenectady, NY. In 1994, he joined Silicon Power Corporation, a former division of General Electric Inc., as the Vice President of Technology. In 1996, he became a Professor at RWTH Aachen University, Aachen, Germany, where he currently leads the Institute for Power Electronics and Electrical Drives. Since 2006, he has been the Director of the E.ON Energy Research Center, RWTH Aachen University. Dr. De Doncker was the President of the IEEE Power Electronics Society (PELS) in 2005 and 2006. He was the founding Chairman of the German IEEE Industry Applications Society PELS Joint Chapter. In 2002, he was the recipient of the IEEE IAS Outstanding Achievement Award. In 2008, he received the IEEE PES Nari Hingorani Custom Power Award. In 2009, he led a VDE/ETG Task Force on Electric Vehicles. In 2010, he received an honorary doctor degree of TU Riga, Latvia. In 2013, he received the IEEE William E. Newell Power Electronics Award.